ELSEVIER

Contents lists available at ScienceDirect

## Journal of Power Sources

journal homepage: www.elsevier.com/locate/jpowsour





# Sb@Ni<sub>6</sub> superstructure units stabilize Li-rich layered cathode in the wide voltage window

Bo Cao <sup>a,1</sup>, Yiwei Li <sup>a,1</sup>, Mingjian Zhang <sup>a,\*</sup>, Ningyan Cheng <sup>b</sup>, Ming Shen <sup>c</sup>, Bingwen Hu <sup>c</sup>, Jianyuan Li <sup>a,d</sup>, Zhibo Li <sup>a</sup>, Shenyang Xu <sup>a</sup>, Wenguang Zhao <sup>a</sup>, Ni Yang <sup>a</sup>, Junliang Sun <sup>d</sup>, Shixue Dou <sup>b</sup>, Yang Ren <sup>e</sup>, Haibiao Chen <sup>f</sup>, Liang Yin <sup>e,\*\*</sup>, Feng Pan <sup>a,\*\*\*</sup>

- <sup>a</sup> School of Advanced Materials, Peking University, Shenzhen Graduate School, Shenzhen, 518055, PR China
- b Institute for Superconducting and Electronic Materials (ISEM), Australian Institute for Innovation Materials (AIIM), University of Wollongong, Wollongong, NSW, 2525. Australia
- <sup>c</sup> Shanghai Key Laboratory of Magnetic Resonance, State Key Laboratory of Precision Spectroscopy, School of Physics and Electronic Science, East China Normal University, Shanghai, 200241, PR China
- <sup>d</sup> College of Chemistry and Molecular Engineering, Peking University, Beijing, 100871, PR China
- X-ray Science Division, Argonne National Laboratory, Lemont, IL, USA
- f Institute of Marine Biomedicine, Shenzhen Polytechnic, Shenzhen, 518055, PR China

#### HIGHLIGHTS

- The performance decay mechanism of Li-rich cathodes in 1.0-4.8 V is revealed.
- Introducing Sb@Ni6 superstructure units enhances the cycling stability.
- The modified oxygen environments suppress the irreversible structural transition.

## ARTICLE INFO

#### Keywords: Li-ion batteries A wide voltage window Li-rich layered cathode Electrochemical degradation Superstructure units

## ABSTRACT

In the practical operations of Li-ion batteries, inevitable deep charge/discharge happens locally due to the intrinsic (de)lithiation inhomogeneity at the electrode and particle level, which would damage the health of batteries and even cause the safety concern. It is essential to develop the stable cathodes operating in a wide voltage window to ensure the health and safety of Li-ion batteries. Herein, we comprehensively investigate the charge/discharge behaviors of a representative Li-rich cathode Li<sub>1.2</sub>Mn<sub>0.54</sub>Ni<sub>0.13</sub>Co<sub>0.13</sub>O<sub>2</sub> in a wide voltage window of 1.0–4.8 V, and reveal that, deep-lithiation would drive violent TM migration and severe Li/TM mixing, thereby leading to the irreversible structural transformation from layered to spinel then to rock salt, eventually causing the fast decay in electrochemical performance. Based on these understandings, a novel Li-rich cathode Li[Li<sub>1</sub>/4Mn<sub>1/2</sub>Ni<sub>1</sub>/6Sb<sub>1/12</sub>]O<sub>2</sub> is successfully synthesized through introducing aromatic Sb@Ni<sub>6</sub> superstructure units in the TM layers. The introduced Sb@Ni<sub>6</sub> superstructure units can effectively tune the local oxygen environment, suppress TM migration, and stabilize the layered framework under deep lithiation. Finally, a stable charge/discharge is achieved in 1.0–4.8 V. This work deepens the understanding into the structural stability of Li-rich cathodes in a wide voltage window, and benefits the development of high-energy-density and safe cathodes.

E-mail addresses: zhangmi@pkusz.edu.cn (M. Zhang), lyin@anl.gov (L. Yin), panfeng@pkusz.edu.cn (F. Pan).

<sup>\*</sup> Corresponding author.

<sup>\*\*</sup> Corresponding author.

<sup>\*\*\*</sup> Corresponding author.

<sup>&</sup>lt;sup>1</sup> These authors contributed equally to this work.

#### 1. Introduction

In recent years, rechargeable lithium ion batteries (LIBs) have been widely equipped in portable electronic devices and electric vehicles. In the next-generation LIB systems, pursuing higher energy density and better security is imminent [1-3]. The energy density of LIB is largely determined by the electrode materials, especially the cathode materials [4]. Li-rich layered oxides, written as  $xLi_2MnO_3 \cdot (1-x)LiMO_2$  (M = Mn, Ni, Co, Fe, etc.), have been regarded as one of the most promising cathode materials due to the high specific capacity (>250 mA h g<sup>-1</sup>) and energy density (>900 W h Kg<sup>-1</sup>) [5,6]. However, there are still some drawbacks hindering the commercialization of these materials, including the low initial Coulombic efficiency, the poor rate performance, the fast degradation of voltage and capacity during cycling, etc. [7–9] These issues have been partly solved by various strategies, such as element doping, surface coating and morphology design through recent research efforts [10-12]. In comparison, only very limited works have been focused on the deep charge/discharge behaviors, which is closely related to increasing the capacity further and improving the battery

Owing to the inhomogeneous structure of a practical electrode, it is expected that the near-surface parts of the electrode are more deeply (de)lithiated than the deep parts. Localized over-(de)lithiation can be harmful to the electrode materials, thus restricting further capacity release and full utilization of energy density [13]. Thackeray's group was the first to study the behavior of a few of layered cathodes,  $xLiMn_{0.5}Ni_{0.5}O_2$ . $(1-x)Li_2TiO_3$ ,  $Li_xMn_{0.5}Ni_{0.5}O_2$ , and  $xLiNiO_2$ .(1-x)Li<sub>2</sub>RuO<sub>3</sub>, under charge/discharge in a wide voltage window in 2002 and 2003 [14–16]. They found that excess Li <sup>+</sup> insertion would cause severe capacity degradation. The origin of the degradation was ascribed to the phase transformation to a deeply lithiated Li<sub>2</sub>MO<sub>2</sub> layered phase with space group  $P\overline{3}m1$ , usually called as 1T phase wherein Li ions locate at the tetrahedral sites [17-19]. Accompanying with the 1T phase, antiphase domain boundaries formed and hindered Li<sup>+</sup> diffusion [20]. Besides, the formation of 1T phase led to large irreversible volume expansion, thus resulting into high lattice strains and even cracks during long-term cycling, causing a severe decrease in the cycling stability of the cathodes [17]. Until 2020, Tarascon's group observed the fast capacity decay during the charging/discharging of a typical layered Li-rich cathode  $Li_{1.2}Mn_{0.54}Ni_{0.13}Co_{0.13}O_2$  (LMR) in a wide voltage window of 1.2-4.8 V [21]. However, the actual reason for the fast performance degradation of LMR was not mentioned. The related reports are summarized in Table S1. In one word, it is known that Li-rich layered cathodes would degrade quickly when cycling in a wide voltage window, while the underlying mechanism has not been thoroughly studied, not to mention a solution to the issue.

The electrochemical performance of a layered oxide cathode is largely determined by the crystal structure. To obtain a novel layered cathode with desired electrochemical performance, it is effective to design the crystal structure from the viewpoint of material gene, specifically utilizing the functional structure units [22]. For example, the unique electrochemical performance of Li-rich cathode greatly depends on the Li@Mn6 superstructure units, in which six MnO6 octahedra are linked in a ring (Mn<sub>6</sub>) with the LiO<sub>6</sub> octahedron at the center. The Sb@Ni6 superstructure unit containing six NiO6 octahedra linked in a ring (Ni<sub>6</sub>) with the SbO<sub>6</sub> octahedron at the center, has been regarded as a stabilizing unit in layered cathodes for sodium ion batteries (SIBs) due to the super-exchange interaction and the degeneration of electronic orbitals [22–24]. The similar function of the Sb@Ni<sub>6</sub> superstructure unit has also been validated in Li-rich layered cathode for LIBs in our previous work [25]. Therefore, to introduce Sb@Ni<sub>6</sub> superstructure units into the layered oxide might be effective to improve the cycling stability in a wide voltage window.

Here, we utilized synchrotron X-ray diffraction (SXRD) and transmission electron microscope (TEM) to explore the mechanism for the

capacity decay of LMR cathode cycled in a wide voltage window of 1.0–4.8 V. It revealed that, severe structure disordering within TM layers and between Li and TM layers occurred when discharged to 1.0 V (the upper panel of Scheme 1), including the disappearance of Li@Mn\_6 superstructure units and the formation of rock-salt domains, which is responsible for the continuous capacity decay of Li-rich cathode. By introducing Sb@Ni\_6 superstructure units in Li\_2MnO\_3 (with only Li@Mn\_6 superstructure units, the lower panel of Scheme 1), we successfully prepared a new Li-rich cathode Li[Li\_{1/4}Mn\_{1/2}Ni\_{1/6}Sb\_{1/12}]O\_2 (LMR-Sb). It exhibited a high reversible capacity of 374 mA h g  $^{-1}$  and an excellent cycling stability due to the stabilized layered structure with the tetrahedral Li  $^+$  storage sites when discharged to 1.0 V. This encouraging result confirmed the role of Sb@Ni\_6 superstructure unit in stabilizing the layered framework in a wide voltage window, which benefits the development of the stable and safe Li-ion batteries.

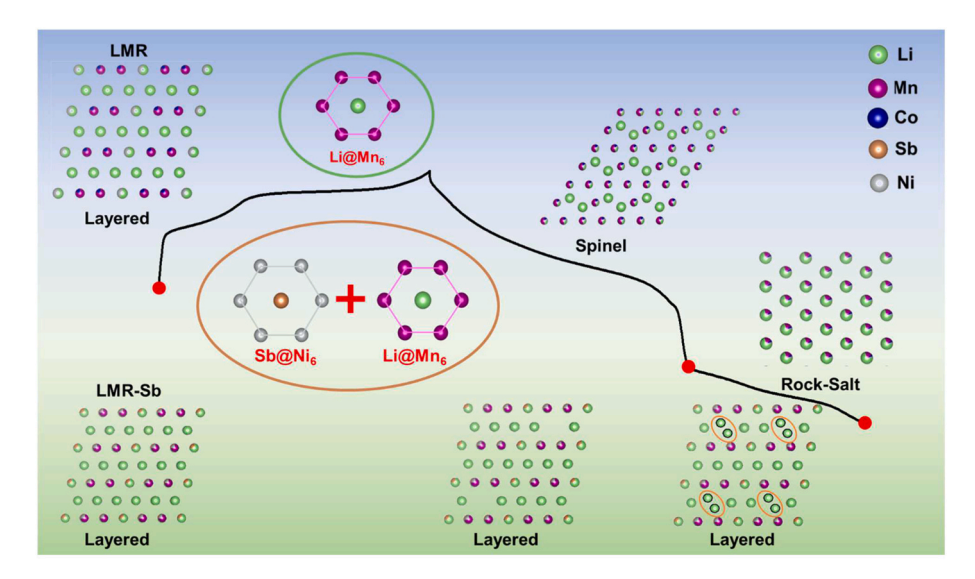
## 2. Materials and methods

## 2.1. Materials preparation

The hydroxide precursor of LMR was purchased from Hai 'an Zhichuan Battery Material Technology Co., Ltd. The precursor was thoroughly mixed with Li<sub>2</sub>CO<sub>3</sub> in a ratio of 1: 1.03 by mechanical grinding, and then the mixture was annealed at 900 °C for 8 h under air atmosphere to obtain the final LMR. The precursor for LMR-Sb was synthesized by sol-gel method. C<sub>2</sub>H<sub>3</sub>O<sub>2</sub>Li-2H<sub>2</sub>O, C<sub>4</sub>H<sub>6</sub>O<sub>4</sub>Ni-4H<sub>2</sub>O, C<sub>4</sub>H<sub>6</sub>O<sub>4</sub>Ni-4H<sub>2</sub>O, and C<sub>6</sub>H<sub>9</sub>O<sub>6</sub>Sb (Sinopharm Chemical Reagent Co., Ltd) were mixed based on the stoichiometric ratio of metal elements in LMR-Sb. Citric acid and polyvinylpyrrolidone (PVP–K30) (Aladdin Reagent Co., Ltd) were used as the chelating agents. The mixed solution was stirred to dry at 90 °C and then annealed at 500 °C for 3 h in the muffle furnace. The obtained precursor was ground in an agate mortar and annealed at 1150 °C for 8 h under air atmosphere.

## 2.2. Materials characterization

The crystal structures of LMR and LMR-Sb at different charge/ discharge states were characterized by laboratory XRD and SXRD. The laboratory XRD data were collected on Bruker D8 Advance diffractometer utilizing Cu- $K\alpha$  radiation ( $K\alpha_1 = 1.54053$  Å and  $K\alpha_2 = 1.54431$  Å) at 45 kV and 100 mA. SXRD data were collected at the 11-ID-C beamline of the Advanced Photon Source (APS) at Argonne National Laboratory using a wavelength of 0.1173 Å. Rietveld refinements of crystal structures were carried out using the General Structure Analysis Software (GSAS) package with the EXPGUI interface [26,27]. The elemental compositions of LMR and LMR-Sb were measured by inductively coupled plasma optical emission spectrometer (ICP-OES). The morphologies of as-prepared samples were characterized by scanning electron microscope (SEM, ZEISS Supra 55 field emission scanning electron microscopy), and the local atomic structure was characterized by transmission electron microscope (TEM, FEI TecnaiG2 F30). The energy dispersive spectrometer (EDS) coupled with SEM was utilized to obtain the element distribution in LMR and LMR-Sb. X-ray photoelectron spectra (XPS, ESCALAB 250XL) was used to analyze the element valance states for the samples at different charge/discharge states, which were etched by Ar<sup>+</sup> ions for 60 s and 120 s for the powders and the electrodes, respectively. All the obtained spectra were corrected by C 1s signal at 284.6 eV. Continuous rotation electron diffraction (cRED) datasets of LMR-Sb were collected by JEOL JEM-1230 microscope operating at 60 kV, under a 15 cm camera length. The range of the collection angle was a minimum collection angle of  $-30^{\circ}$ - $30^{\circ}$ , with a Medipix3 detector. High resolution scanning TEM (STEM) images were obtained using a JEOL ARM-200CF operated at 200 kV. To ensure Z contrast, high angle annular dark-field (HAADF) images were acquired with inner and outer collection angles of 68 and 280 mrad, respectively. <sup>7</sup>Li MAS NMR experiments were performed to analyze the local environments of Li ions



Scheme 1. The structure changes of Li-rich layered cathodes in the wide voltage range.

on a 400 MHz Bruker ADVANCE III spectrometer at  $^7\text{Li}$  Larmor frequency of 155.51 MHz with a triple-resonance 1.9 mm MAS probe. The MAS frequency was 40 kHz and the probe temperature was controlled at 323 K.  $^7\text{Li}$  MAS NMR spectra were all acquired using pj-MATPASS pulse sequence with a  $\pi/2$  pulse length of 1.6  $\mu$ s and a recycle interval of 50 ms. All the  $^7\text{Li}$  shifts were calibrated with respect to 1 M LiCl solution (0 ppm).

## 2.3. Electrochemical measurement

Active materials, acetylene black, and polyvinylidene fluoride (PVDF) were mixed in a weight ratio of 7:2:1 and poured into N-methyl pyrrolidone (NMP). Then the mixture was continuously stirred for 10 h to obtain a smooth slurry. Then the slurry was casted on a carbon-coated Al foil and dried in a vacuum oven at 110 °C. Coin cells (CR2032) were assembled in an argon-filled glove box where the contents of water and oxygen were below 1 ppm. Pure lithium foil and polymer membrane were used as the counter electrode and the separator, respectively. The electrolyte was 1 M lithium hexafluorophosphate (LiPF6) solution in a mixed solvent with ethylene carbonate (EC) and ethyl methyl carbonate (EMC) in a weight ratio of 2:5. The as-assembled cells were charged and discharged in galvanostatic mode using a NEWARE system. Cyclic voltammetry (CV) results and the electrochemical impedance spectra (EIS) were collected by an electrochemical workstation (1400 cell test system, Solartron).

## 3. Results and discussion

## 3.1. The charge/discharge behaviors of LMR in a wide voltage window

The actual element contents of Li, Mn, Ni, and Co in LMR were determined by ICP-OES (Table S2), and they are consistent with the target values. The XRD pattern of LMR and the corresponding refinement result are shown in Fig. S1a, which reflects a well-crystallized O3-type layered structure with space group C2/m. The superlattice peaks observed in the range of  $20\text{--}30^\circ$ , correspond to the Li@Mn\_6 super-structure units in Li\_2MnO\_3 component. The detailed structural parameters from the Rietveld refinement are shown in Table S3. The SEM image (Fig. S1b) presents the morphology of the irregular-shape secondary particles with the diameter of around 1  $\mu$ m, composited by the primary particles around 300 nm.

To investigate the influence of charge/discharge in a wide voltage window on the electrochemical performance, both a regular voltage window of 2.0-4.8 V and a wider voltage window (1.0-4.8 V) were chosen. Fig. 1a presents the capacity-voltage profiles at different cycles in 2.0-4.8 V. A long plateau above 4.5 V is observed in the charge branch of the 1st cycle, implying the oxygen activation process. Severe capacity fading with the capacity retention of 74% and voltage drop of 0.27 V are observed within 50 cycles. For comparison, the capacity-voltage profiles in 1.0–4.8 V are shown in Fig. 1b. An extra specific capacity of 206 mA h g<sup>-1</sup> is obtained in 1.0-2.0 V, delivering an ultrahigh total capacity of 501 mA h g<sup>-1</sup>, corresponding to the formula Li<sub>1.75</sub>Mn<sub>0.54</sub>Ni<sub>0.13</sub>Co<sub>0.13</sub>O<sub>2</sub> in the end of discharge. However, the capacity retention is only 62%, and the average discharge voltage decreases by 0.72 V after 50 cycles, indicating the aggravated capacity and voltage decay. For further analysis, the entire discharge process is divided into two voltage regions, > 2.0 V and <2.0 V. The capacity decay of each region is plotted as a function of the cycle number in Fig. 1c. About 20% of capacity decay occurs in the first six cycles (marked in the pink ellipse), which takes up half of the total capacity decay within 50 cycles. As indicated by the two similar slopes (marked by two dashed arrows), the decay rate of the total capacity is similar to that of the capacity >2.0 V after the first six cycles. Therefore, the subsequent capacity decay mainly comes from the highvoltage part (>2.0 V). Besides, the capacity decay above 2.0 V during charge/discharge in 1.0-4.8 V is much faster than that during cycling in 2.0-4.8 V (Fig. 1d), indicating the detrimental impact on the highvoltage region (>2.0 V). CV tests were performed to explore the cause of capacity degradation. The region above 2.0 V in the first cycle for the 1.0-4.8 V case is basically identical to that for the 2.0-4.8 V case (Fig. S2). Two oxidation peaks at around 4.20 and 4.61 V are ascribed to TM oxidation and oxygen oxidation, respectively. Upon discharge, a reduction peak is observed around 3.30 V, corresponding to TM reduction hybridizing with a certain extent of oxygen reduction [28]. In the 2.0-4.8 V case (upper panel of Fig. 1e), oxygen oxidation peak shifted to 4.52 V with cycling, and TM oxidation peak shifts to the lower voltage (3.94 V), hinting the complete activation of Li<sub>2</sub>MnO<sub>3</sub> [29]. In addition, a pair of redox peaks at 2.92 and 2.74 V are observed since the 2nd cycle (marked by the grey ellipse), implying the formation of trace spinel structure after the first cycle [30]. The oxidation peak at around 3.2 V gradually intensifies with the cycle number, indicating the growth of the rock-salt phase [31,32]. While tested in 1.0-4.8 V (lower panel of Fig. 1e), another pair of redox peaks at 1.87 and 1.38 V (marked by the green ellipse) could be found. They correspond to the  $\mathrm{Mn}^{3+}/\mathrm{Mn}^{4+}$ redox, confirmed by Mn 2p XPS results in Fig. S3. However, this pair of redox peaks quickly diminish with cycling, well consistent with the capacity degradation below 2.0 V shown in Fig. 1b. The redox peaks

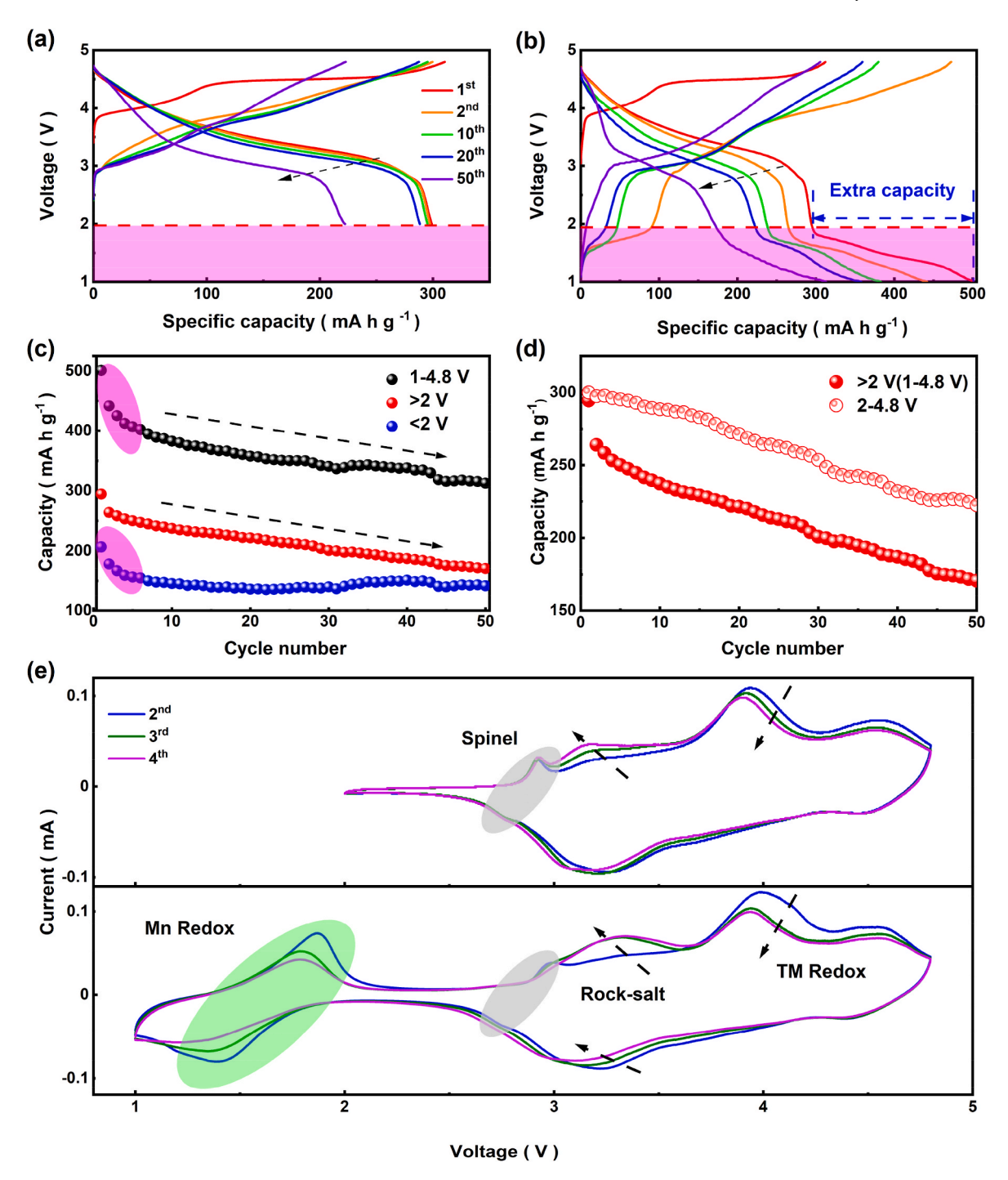


**Fig. 1.** The electrochemical performance of LMR. The capacity-voltage profiles for LMR cathode at the 1st, 2nd, 10th, 20th, and 50th cycle in 2.0–4.8 (a) and 1.0–4.8 V (b). The current density is 20 mA  $\rm g^{-1}$ . (c) The cycling performance of the LMR cathode cycled in 1.0–4.8 V. The overall cycling stability (black dots) is divided into two regions: 2.0–4.8 (red dots) and 1.0–2.0 V (blue dots). The quick capacity decay in the first few cycles is marked by pink circles. (d) The comparison of the cycling stability of LMR cycled in 2.0–4.8 V (hollow red dots) and the 2.0–4.8 V part (red dots) when cycled in 1.0–4.8 V. (e) The corresponding CV curves from the 2nd to 4th cycle in 2.0–4.8 and 1.0–4.8 V. (For interpretation of the references to colour in this figure legend, the reader is referred to the Web version of this article.)

 $(2.98 \, \mathrm{and} \, 2.73 \, \mathrm{V})$  related to the spinel phase appear in the 2nd cycle, but disappear in the subsequent cycles. Concurrently, the oxidation peak  $(3.29 \, \mathrm{V})$  related to the rock salt phase quickly intensifies, hinting the phase transition from layered to spinel then to rock salt. Considering that the decrease of redox peaks below 2.0 V accompanies with the appearance of oxidation peak at 3.29 V, we can deduce that, the fast capacity degradation below 2.0 V may be correlated to the phase transition to the rock-salt phase.

## 3.2. Structural degradation of LMR in a wide voltage window

To validate the above deduction about the structural change, SXRD patterns of LMR cathodes at different charge/discharge states in the 1st cycle are shown in Fig. 2a. No new Bragg peaks are observed, indicating no obvious phase transformation. To examine the subtle changes, two regions marked by the rectangles are enlarged on the right. In the 1st enlarged region, the superlattice peaks  $(020)_M$  and  $(110)_M$  disappear

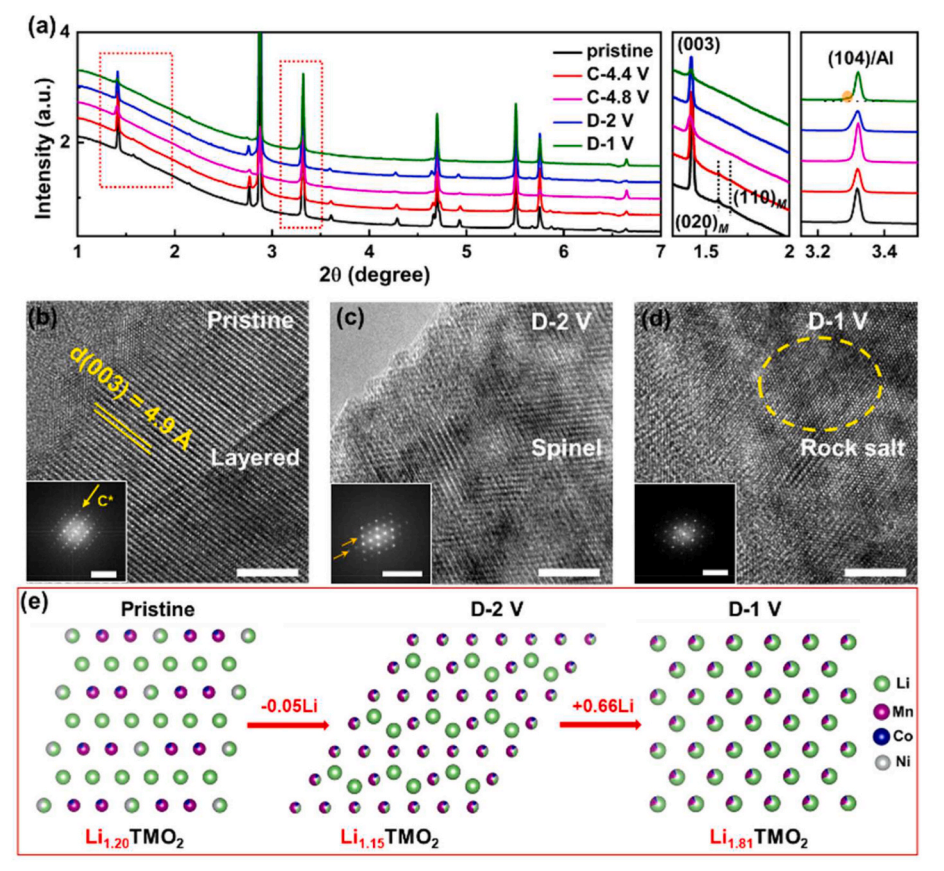


Fig. 2. The structural evolution of LMR during the charge/discharge in a wide voltage window. (a) SXRD patterns of the LMR cathodes before cycling (pristine), charged to 4.4 V (C-4.4 V), charged to 4.8 V (C-4.8 V), discharged to 2.0 V (D-2 V) and discharged to 1.0 V (D-1 V). Two regions marked by the dashed rectangles, 1.3-2.0° and 3.15-3.50°, were enlarged to examine the peak changes. The superlattice peaks  $(020)_M$  and  $(110)_M$  are marked by the dashed lines. (b)-(d) HRTEM images and the corresponding fast Fourier transform (FFT) maps of LMR cathodes before cycling (pristine), discharged to 2.0 V (D-2 V) and discharged to 1.0 V (D-1 V). The scale bars in the HRTEM images and FFT maps are 5 nm and 10 1/nm, respectively. The spinel phase region and the rock-salt phase region are marked in the corresponding HRTEM image by the yellow dashed circle. (e) Schematic illustrations of the structural change of LMR in the first cycle (1.0-4.8 V), from layered phase to spinel phase and finally to disordered rock-salt phase. (For interpretation of the references to colour in this figure legend, the reader is referred to the Web version of this article.)

when charge to 4.8 V and never re-appear even discharged to 1.0 V, implying that the ordering of Li@Mn $_6$  superstructure unit in the TM layers has been destroyed. In the 2nd enlarged region, there is a tiny shoulder on the left of (104)/Al peak (marked by the orange shadow), which may correspond to a new rock salt phase, demonstrated by the TEM results below. Similar phenomenon is observed in XRD patterns in Fig. S4. The (104) peak becomes broader and shifts to the low angle when discharged from 2.0 V to 1.0 V, further demonstrating the formation of a new phase.

To further check the changes in local structure, high-resolution TEM (HRTEM) was performed. As shown in Fig. 2b, the perfect layered structure with an interlayer spacing of 4.9 Å is observed in HRTEM image of LMR before cycling. When charged to 4.8 V, the particle surface partially transforms to spinel phase (marked by an orange circle in Fig. S5a). The observation is consistent with the CV results above and it is caused by oxygen loss and subsequent TM migration at high voltages, contributing to cation mixing in the TM layers (indicated by the disappearance of superlattice peaks in Fig. 2a) [33]. The spinel phase is observed both at the surface (Fig. 2c) and in the bulk (Fig. S5b) when discharged to 2.0 V, hinting the aggravated cationic mixing between the Li layers and the TM layers. When discharged to 1.0 V, the spinel phase further transforms to the rock-salt phase (marked by yellow circles in Fig. 2d and orange circles Fig. S5c, respectively), which is consistent with CV results above. The phase transformation process is summarized in Fig. 2e. Upon further lithiation of 0.66 Li<sup>+</sup>, more Li/TM mixing is introduced in the spinel phase, which induces the formation of a Li-rich rock-salt phase with the complete cationic disordering in all octahedral sites. Figs. S5d-e exhibit HRTEM images of fully charged and discharged LMR cathodes after the 2nd cycle, showing the aggravated phase transition to the spinel phase and rock-salt phase than the 1st cycle. It implies that the phase transformation is only partially reversible, and the structure degradation would occur continuously with cycling.

Combining the electrochemical results and the bulk/local structural

analysis, the severe capacity decay (especially in the initial few cycles) when cycling in a wide voltage window could be ascribed to the irreversible phase transformation due to over-lithiation below 2.0 V. The cationic disordering in the rock-salt phase blocks the pathway of  ${\rm Li}^+$  migration, and reduces the amount of available Li ions for reversible (de)intercalation, leading to a significant capacity degradation with cycling in LMR cathode.

## $3.3. \ \textit{Li-rich layered oxide containing Sb} @Ni_6 \ \textit{superstructure units}$

From the aspect of material genes [34–36], we plan to introduce a more stable Sb@Ni $_6$  superstructure unit into the TM layers to improve the structural stability of Li-rich layered oxides. The structural design is shown in Fig. 3a. Li[Li $_{1/3}$ Mn $_{2/3}$ ]O $_2$  and Li[Sb $_{1/3}$ Ni $_{2/3}$ ]O $_2$  exhibit the similar layered structure with Li layers and TM layers alternately stacking along the c axis. The only difference is that, the TM layer of Li [Li $_{1/3}$ Mn $_{2/3}$ ]O $_2$  is composed of Li@Mn $_6$  superstructure units, while the TM layer of Li[Sb $_{1/3}$ Ni $_{2/3}$ ]O $_2$  is composed of Sb@Ni $_6$  superstructure units (marked by hexagons). Therefore, it is possible to mix Li@Mn $_6$  and Sb@Ni $_6$  together in the TM layers to create a series of new layered solid-solution materials. Here we chose a ratio of 3:1 between Li@Mn $_6$  and Sb@Ni $_6$  to do experimental examination.

The product (denoted as LMR-Sb) was prepared through a sol-gel method and subsequent calcination (see details in Experimental section). The actual contents of Li, Mn, Ni, and Sb elements measured by ICP technique are well consistent with our design (Table S2). SEM images (Figs. S6a-b) exhibit the irregular and severely agglomerated primary particles of 2–3  $\mu$ m. The SEM EDX mapping results (Figs. S6c-f) demonstrate the uniform elemental distribution of Mn, Ni and Sb in LMR-Sb. XPS spectra of Mn, Ni, Sb, and O are shown in Fig. S7. Mn  $2p_{3/2}$  and Ni  $2p_{3/2}$  peaks are located at around 642.2 and 854.8 eV, respectively, indicating the presence of Mn<sup>4+</sup> and Ni<sup>2+</sup> at the particle surface [37]. The peak positions do not change with the etching time,

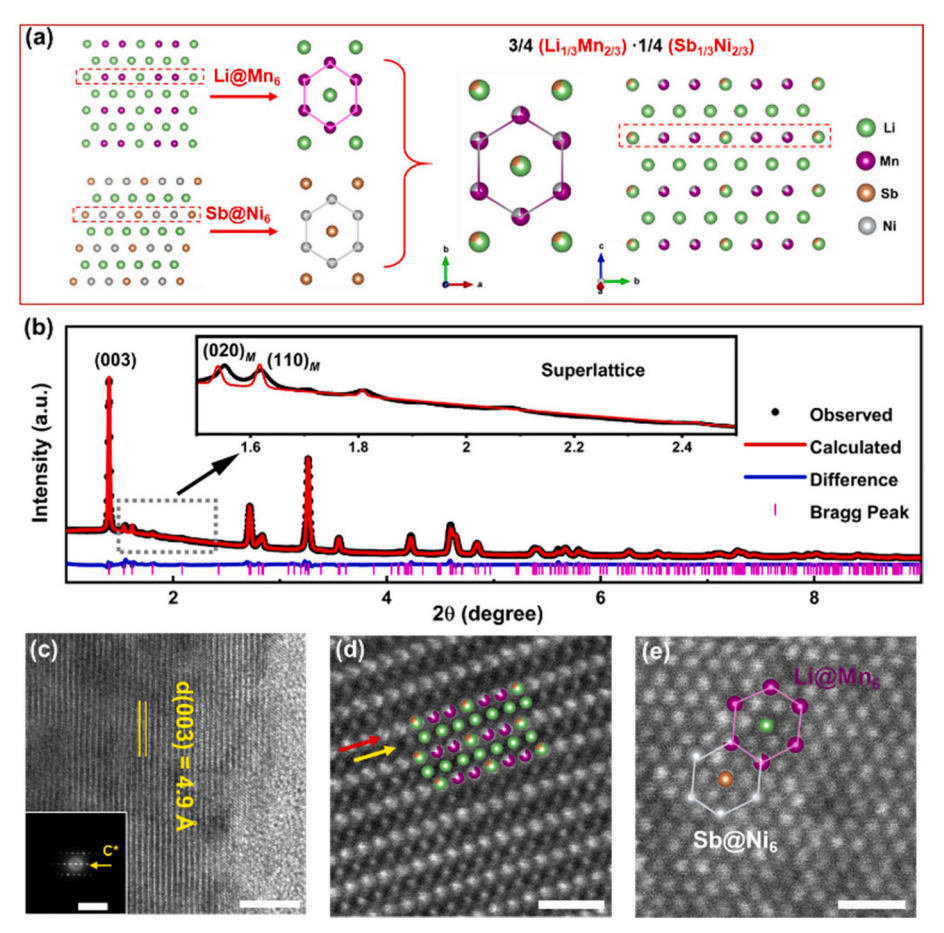


Fig. 3. The design and structural characterization of LMR-Sb. (a) Schematic illustration of the design of a new layered oxide LMR-Sb by compositing Li@Mn<sub>6</sub> and Sb@Ni6 superstructure units in TM layers. (b) SXRD pattern and the corresponding Rietveld refinement of as-prepared LMR-Sb. The superlattice peaks are marked by grey dashed rectangle and magnified in the inset. (c) HRTEM image and the corresponding FFT (inset) of LMR-Sb. The scale bars in HRTEM images and FFT maps are 5 nm and 10 1/nm, respectively. (d) HAADF-STEM image of LMR-Sb of the ac plane. The scalebar is 1 nm. TM slab and Li slab are marked by red and yellow arrows, respectively. (e) HAADF-STEM image of LMR-Sb of the ab plane. The scale bar is 0.5 nm. Li@Mn6 and Sb@Ni6 superstructure units are marked by the purple and silvery hexagons, respectively. (For interpretation of the references to colour in this figure legend, the reader is referred to the Web version of this article.)

demonstrating the constant valence states for  $\mathrm{Mn^{4+}}$  and  $\mathrm{Ni^{2+}}$  with the depth. A peak around 531.5 eV in the O 1s spectra could be observed before etching and disappeared after etching, implying that a small amount of  $\mathrm{Li_2CO_3}$  formed at the surface [38]. The peak around 538.5 eV in the Sb 3d spectra corresponded to  $\mathrm{Sb^{5+}}$  [39].

The crystal structure of LMR-Sb was analyzed using SXRD, selected area electron diffraction (SAED), and STEM. As shown in Fig. 3b, SXRD pattern can be well refined with the typical layered structure model with space group C2/m, which is consistent with our design. The presence of superlattice peaks in the zoom-in inset indicate the preservation of the six-member ring superstructure units. The superlattice peaks are broader than the refined peaks, which suggests the mixing of Li@Mn<sub>6</sub> and Sb@Ni<sub>6</sub> superstructure units in the TM layers. The detailed structure parameters are shown in Table S3. Larger lattice parameters are due to the larger ionic radius of  $\mathrm{Sb^{5+}}$  (0.6 Å) and  $\mathrm{Ni^{2+}}$  (0.69 Å) than those of  $Co^{3+}$  (0.545 Å) and  $Mn^{4+}$  (0.53 Å). Moreover, a higher degree of cationic mixing (around 0.07) was induced in the Li layers of LMR-Sb compared to that of LMR (around 0.03). The three-dimension electron diffraction images of a selected LMR-Sb particle (Fig. S8a) are shown in Figs. S8b-d from  $b^*$ ,  $a^*$ , and  $c^*$  direction, respectively. The diffraction results confirm the well layered structure since no additional diffraction spots is observed. It implies that, Sb@Ni6 superstructure units are introduced in the solid-solution form. HRTEM image of LMR-Sb in Fig. 3c also exhibits a well crystallized layered phase along the c direction, with the corresponding (003) interplanar spacing of around 4.9 Å. In some particles, a small fraction of spinel structure is observed at the particle surface (Fig. S9), which can be related to the electrochemical behavior discussed below. To further clarify the local structure, STEM images were taken along the ac plane and the ab plane. As shown in Fig. 3d-e, the bright-and-dark alternating slabs along the c axis correspond to the TM slab (red arrow) and the Li slab (yellow arrow),

respectively. Nevertheless, the relatively low contrast between the Li and TM slabs implies a small degree of Li/TM mixing, consistent with the refinement result of SXRD pattern (Table S3). For the ab plane (Fig. 3e and Fig. S10), Li@Mn6 and Sb@Ni6 superstructure units (marked by the purple and silvery hexagons) can be distinguished according to the different contrast of the center Li and Sb atoms. The image further confirms that the distribution of Sb@Ni6 and Li@Mn6 superstructure units in the TM layers of LMR-Sb is relatively uniform. It is consistent with the solid-solution phase demonstrated by the above SXRD result.

## 3.4. Stable charge/discharge of LMR-Sb in a wide voltage window

The effect of the introduced superstructure unit on the electrochemical performance of LMR-Sb was systemically evaluated (Fig. 4). Fig. 4a displays the capacity-voltage profiles of LMR-Sb in 1.0-4.8 V at different cycles. In the 1st cycle, an oxygen oxidation plateau above 4.5 V becomes much shorter compared to that of LMR (Fig. 1a-b). This might be attributed to the reduced oxygen redox activity, arising from the modified local oxygen environments by the introduction of Sb@Ni<sub>6</sub> superstructure units [25]. LMR-Sb exhibits a high capacity of 374 mA h  $\rm g^{-1}$  and a high energy density of 908 W h kg $^{-1}$ . Thereinto, the region below 2.0 V contributes around 197 mA h  $\rm g^{-1}$ , nearly half of the total capacity. Different from LMR (Fig. 1b), the capacity and the average discharge voltage below 2.0 V do not change noticeably with cycling. It indicates that, the structural stability is greatly improved by introducing Sb@Ni<sub>6</sub> superstructure units. In addition, the voltage decay above 2.0 V is also suppressed, giving a decrease of 0.25 V (vs. 0.42 V of LMR) after 50 cycles. It hints that, TM migration in the TM layers is partially inhibited.

The CV curves of LMR-Sb in the first four cycles are shown in Fig. 4b.

Li<sub>1,25</sub>TMO<sub>2</sub>

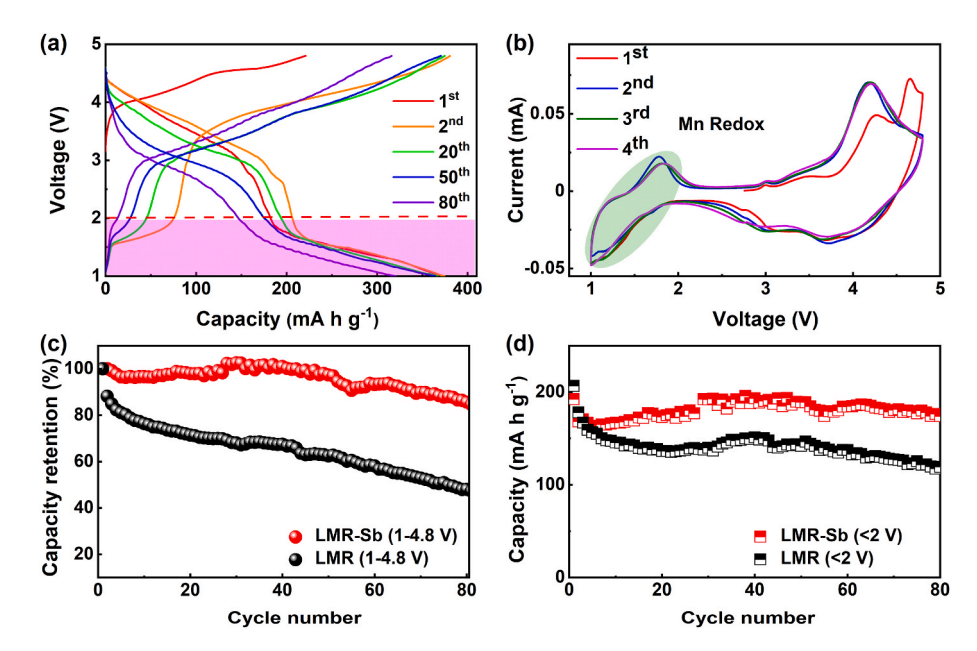
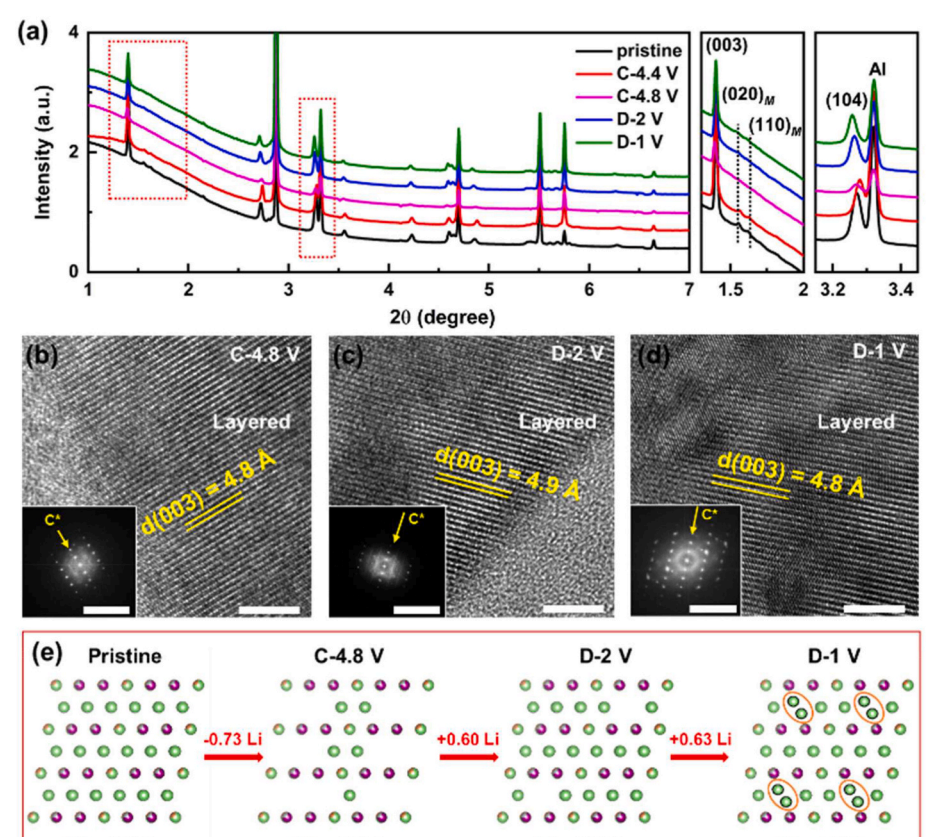


Fig. 4. The electrochemical performance of LMR-Sb. (a) The capacity-voltage profiles of LMR-Sb of the 1st, 2nd, 20th, 50th, and 80th cycle in the voltage range of 1.0–4.8 V at the current density of 20 mA  $g^{-1}$ . (b) The CV curves of LMR-Sb during the initial four cycles in 1.0–4.8 V. The cycling performance comparison of LMR and LMR-Sb in 1.0–4.8 V (c) and the part below 2.0 V (d) at 20 mA  $g^{-1}$ .

Two oxidation peaks are observed at 4.15 and 4.65 V in the 1st cycle, corresponding to Ni oxidation and oxygen oxidation, respectively. The intensity of the latter is much lower than that for LMR (Fig. 1e), which is consistent with the short charge plateau of oxygen oxidation in the capacity-voltage curves. A pair of oxidation/reduction peaks are observed at 1.78 and 1.06 V. Different from that for LMR, this pair of

Li<sub>0.52</sub>TMO<sub>2</sub>

peaks almost do not change with cycling, consistent with the stable cycling below 2.0 V. In addition, a pair of tiny peaks at around 2.90 V could be observed in the first cycle and the following cycles, and they can be related to the formation of spinel phase at the surface of LMR-Sb (Fig. S9). The XPS spectra at different charge/discharge states are shown in Fig. S11. Mn  $2p_{3/2}$  peak only shifts to lower binding energy when



**Fig. 5.** The structural evolution of LMR-Sb during the charge/discharge in a wide voltage window. (a) *Exsitu* SXRD patterns for LMR-Sb with different charge/discharge states, including pristine, charge to 4.4 V (C-4.4 V), charge to 4.8 V (C-4.8 V), discharge to 2 V (D-2 V) and discharge to 1.0 V (D-1 V). Two regions marked by the dashed rectangles, 1.3–2.0° and 3.15–3.45°, were enlarged to examine the peak changes. (b)–(d) HRTEM images and the corresponding fast Fourier transform (FFT) of LMR-Sb cathode charged to 4.8 V (C-4.8 V), discharged to 2.0 V (D-2 V) and discharged to 1.0 V (D-1 V). (e) Schematic diagram of the structural evolution of LMR-Sb during charge/discharge in 1.0–4.8 V.

Li<sub>1.75</sub>TMO<sub>2</sub>

Li<sub>1.12</sub>TMO<sub>2</sub>

discharged from 2.0 to 1.0 V, implying that the pair of redox peaks below 2.0 V in CV curves (Fig. 4b) are partially ascribed to Mn redox, similar with the behavior of LMR.

The cycling stability of LMR-Sb and LMR are compared in Fig. 4c–d. Although the initial discharge capacity of LMR is higher, the capacity of LMR-Sb was much more stable with cycling. After 80 cycles, LMR-Sb maintained a capacity of 321 mA h g $^{-1}$ , equivalent to a much higher retention of 86% than that of LMR (48%). Notably, the good cycling stability below 2.0 V is also confirmed in LMR-Sb with a capacity retention of 88%.

In brief, through combining  $\text{Li@Mn}_6$  and  $\text{Sb@Ni}_6$  superstructure units, reversible cycling in a wide voltage range (1.0–4.8 V) has been realized in LMR-Sb, better than most known layered oxides (Table S1).

## 3.5. Mechanism for the stable charge/discharge in a wide voltage window

To identify the structural origin of the excellent cycling performance of LMR-Sb in such a wide voltage range, *in-situ* and *ex-situ* SXRD experiments were performed to track the structural evolution during the first cycle. *Ex-situ* SXRD patterns at different charge/discharge states are shown in Fig. 5a. No new peak is observed when discharged from 2.0 V to 1.0 V, which is different with the behavior of LMR, indicating that, the layered structure of LMR-Sb is reserved in the whole voltage range. To further examine the structure changes, two regions marked by the red dashed rectangles are enlarged. The superlattice peaks could be partially

recovered when discharged to 2.0 V and even to 1.0 V, and similar results are observed in the laboratory XRD data (Fig. S12), confirming that cationic ordering in the TM layers was stable in LMR-Sb under charge/ discharge in a wide voltage window. The local structure of LMR-Sb at different charge/discharge states are shown in Fig. 5b-d and S13. When charged to 4.8 V (Fig. 5b), LMR-Sb maintains a well-defined layered structure, in contrast to LMR where spinel phase is observed at the particle surface. When further discharged to 2.0 and 1.0 V, the layered structure still survives both at the surface (Fig. 5c-d) and in the bulk (Figs. S13a-b). No obvious difference can be observed when discharged from 2.0 to 1.0 V, well consistent with the SXRD results. Even after the 2nd cycle, no phase transformation can be found at the surface of LMR-Sb (Figs. S13c-d), further confirming the stable layered structure. To probe the local configuration of Li ions under different discharge states, <sup>7</sup>Li magic-angle spinning (MAS) nuclear magnetic resonance (NMR) spectroscopy was performed. In Fig. S14, a small resonance appears at 525 ppm, whose position is consistent with that for LiMn<sub>2</sub>O<sub>4</sub> with the tetrahedral coordinated Li ions. It indicates that, extra Li ions are inserted into the tetrahedral sites without causing serious cation mixing when discharged to 1.0 V. The structural models are illustrated in Fig. 5e, which explain the superb stability of LMR-Sb.

To analyze the structure evolution during charge/discharge, *in-situ* SXRD during the first cycle of LMR-Sb was conducted. As shown in Fig. 6a, the (003) peak does not shift noticeably during the cycle, indicating the small change along the c axis. The (104) peak continuously

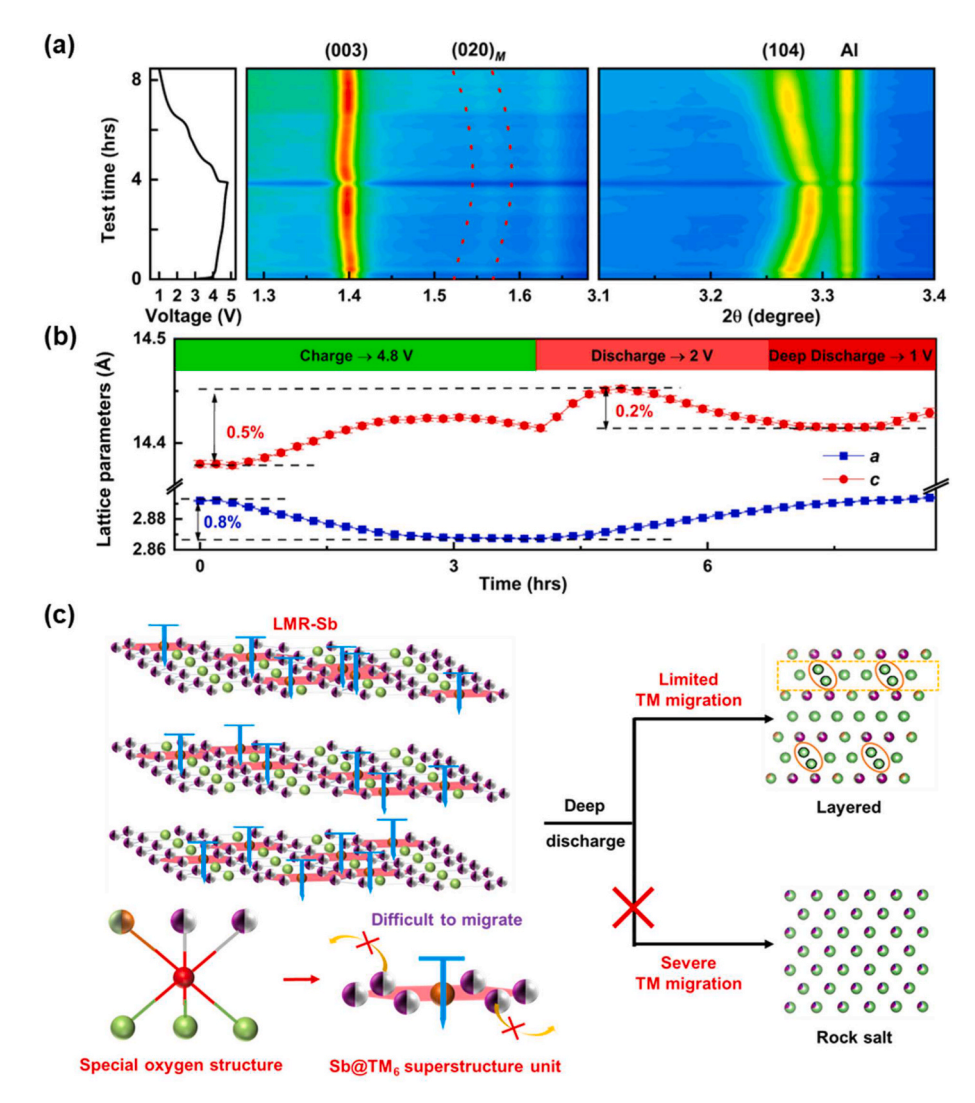


Fig. 6. *In-situ* SXRD of LMR-Sb and the schematic illustration. (a) *In-situ* SXRD patterns of LMR-Sb during the 1st cycle. The superlattice peaks are marked between two dashed curves. (b) Evolution of the lattice parameters as a function of state of charge/discharge. The values were obtained from Rietveld refinement of *in-situ* SXRD data. (c) Schematic illustration showing Sb@Ni<sub>6</sub> superstructure units serve as T-pins fixing the oxygen framework to ensure the structural stability of Li-rich cathode.

shifts to high angle during charge and to low angle during discharge, hinting the contraction and expansion in the ab plane during charge/ discharge, respectively. These changes in the ab plane should be related to the changes in the TM-O bond length due to TM redox. Moreover, the superlattice peak  $(020)_M$  (between the dashed lines) shifts in a similar trend like the (104) peak, suggesting that the superstructure units in TM layers are maintained during charge/discharge. We performed Rietveld refinement to quantify the structure changes (Fig. 6b). Parameter a decreases by 0.8% after charge and returns to the original value after discharge, like most layered oxide materials [13,17,40,41]. The change should be correlated with the elongating and shortening of the TM-O bond length due to the valence changes of Ni/Mn cations. During charge, c first increases by 0.3% with TM oxidation, then decreases a little (around 0.1%) with oxygen oxidation. The trend is consistent with that of other layered oxides, and the change extent is the smallest as far as we know [28,42,43], which should be correlated with the stable Sb@Ni<sub>6</sub> superstructure units. During discharge, c first increases by 0.2% due to Li insertion, then decreases by the similar extent till 2.0 V. When further discharged to 1.0 V, only 0.1% of increase in c is observed, as a large amount of Li<sup>+</sup> are inserted to give an extra capacity of 197 mA h  $g^{-1}$ . Overall, the changes of a and c are both around 0.2% below 2.0 V, much smaller than the changes (>1%) in conventional Li-rich cathodes due to during the formation of 1T phase [15,17,19]. The changes in the lattice parameters are also small during the 2nd cycle (Fig. S15). In addition, ex-situ XRD patterns and HRTEM images of LMR-Sb after 2 cycles, 5 cycles, 10 cycles, 20 cycles, 50 cycles and 70 cycles were taken to examine the structural stability in Figs. S16 and S17. The layered structure is well maintained and no extra phase is observed even after 50 cycles, demonstrating that the good structural stability after long-term cycling. After 70 cycles, there are a small amount of spinel and rock-salt phases formed at the particle surface (Fig. S17g), which may be responsible for the slight capacity degradation upon the prolonged cycling in Fig. 4c.

Finally, the role of Sb@Ni $_6$  superstructure unit in LMR-Sb cathode is illustrated in Fig. 6c. The introduced Sb@Ni $_6$  superstructure units could modify the local oxygen structure and make the anionic framework become much stable [25,36]. In the stable anionic framework, Sb@Ni $_6$  superstructure units work as pins (the blue T-pins in the drawing), preventing the migration of TM cations. Thus, the structure ordering can be strongly held in place. When deeply discharged, the stable anionic framework is stable to accommodate the excess Li ions in the tetrahedral sites. Since the undesirable phase transition to rock salt phase is greatly inhibited, the material can deliver an excellent cycling stability in a wide voltage window.

## 4. Conclusions

The electrochemical behavior and the corresponding structural evolution of the LMR cathode in a wide voltage window (1.0-4.8 V) were comprehensively studied in this work. The results reveal that, the fast electrochemical decay of LMR can be ascribed to the irreversible structure transformation from layered to spinel and rock salt due to serious cationic disordering. As a novel solution, we introduced a new Li-rich layered oxide LMR-Sb by combining Li@Mn6 and Sb@Ni6 superstructure units in the TM layers to stabilize the layered structure. The introduced Sb@Ni6 superstructure units can effectively tune the local oxygen environment and serve as pins to suppress TM migration, thus stabilizing the layered framework under deep-lithiation and successfully restricting the structure transition to rock-salt phase. As a result, LMR-Sb exhibited a high capacity of 374 mA h g<sup>-1</sup> and a good cycling performance in a wide voltage range (1.0–4.8 V). These findings provide a indepth understanding of the structural origin of the performance decay in Li-rich layered oxide cathodes when cycling in a wide voltage window. More importantly, we demonstrate a new approach to effectively improve the structural stability of Li-rich layered cathodes from the perspect of superstructure units.

#### CRediT authorship contribution statement

Bo Cao: Conceptualization, Investigation, Visualization, Methodology, Formal analysis, Writing – original draft. Yiwei Li: Conceptualization, Investigation, Visualization, Methodology, Formal analysis, Writing – original draft. Mingjian Zhang: Conceptualization, Investigation, Visualization, Formal analysis, Writing – review & editing. Ningyan Cheng: Resources. Ming Shen: Resources. Bingwen Hu: Resources. Jianyuan Li: Resources. Zhibo Li: Investigation. Shenyang Xu: Investigation. Wenguang Zhao: Investigation. Ni Yang: Investigation. Junliang Sun: Resources. Shixue Dou: Resources. Yang Ren: Resources. Haibiao Chen: Writing – review & editing. Liang Yin: Writing – review & editing, Supervision, Project administration, Funding acquisition.

## **Declaration of competing interest**

The authors declare that they have no known competing financial interests or personal relationships that could have appeared to influence the work reported in this paper.

## Data availability

No data was used for the research described in the article.

## Acknowledgements

This work was financially supported by the National Natural Science Foundation of China (52172175), the Shenzhen Science and Technology Research Grant (JCYJ20210324130812033, JCYJ20200109140416 788), the Basic and Applied Basic Reuter Foundation of Guangdong Province (No. 2021B1515130002), the Chemistry and Chemical Engineering Guangdong Laboratory (1922018), the National Key R&D Program of China (2020YFB0704500), and the Major Science and Technology Infrastructure Project of Material Genome Big-science Facilities Platform supported by Municipal Development and Reform Commission of Shenzhen. This research used resources of the Advanced Photon Source, a U.S. Department of Energy (DOE) Office of Science User Facility operated for the DOE Office of Science by Argonne National Laboratory under Contract No. DE-AC02-06CH11357.

## Appendix A. Supplementary data

Supplementary data to this article can be found online at https://doi. org/10.1016/j.jpowsour.2022.232148.

## References

- K. Mizushima, P.C. Jones, P.J. Wiseman, J.B. Goodenough, Mater. Res. Bull. 15 (1980) 783–789.
- [2] Y.-K. Sun, D.-J. Lee, Y.J. Lee, Z. Chen, S.-T. Myung, ACS Appl. Mater. Interfaces 5 (2013) 11434–11440.
- [3] H.-J. Noh, S. Youn, C.S. Yoon, Y.-K. Sun, J. Power Sources 233 (2013) 121–130.
- [4] S.K. Martha, H. Sclar, Z.S. Framowitz, D. Kovacheva, N. Saliyski, Y. Gofer, P. Sharon, E. Golik, B. Markovsky, D. Aurbach, J. Power Sources 189 (2009) 248–255.
- [5] Z.H. Lu, D.D. MacNeil, J.R. Dahn, Electrochem. Solid State Lett. 4 (2001) A191–A194.
- [6] J.R. Croy, M. Balasubramanian, K.G. Gallagher, A.K. Burrell, Accounts Chem. Res. 48 (2015) 2813–2821.
- [7] P.K. Nayak, J. Grinblat, M. Levi, B. Markovsky, D. Aurbach, J. Electrochem. Soc. 161 (2014) A1534–A1547.
- [8] R. Shunmugasundaram, R.S. Arumugam, J.R. Dahn, Chem. Mater. 27 (2015) 757–767.
- [9] X. Yu, Y. Lyu, L. Gu, H. Wu, S.-M. Bak, Y. Zhou, K. Amine, S.N. Ehrlich, H. Li, K.-W. Nam, X.-Q. Yang, Adv. Energy Mater. 4 (2014), 1300950.
- [10] X. Feng, Y. Gao, L. Ben, Z. Yang, Z. Wang, L. Chen, J. Power Sources 317 (2016) 74–80.
- [11] M.-J. Wang, F.-D. Yu, G. Sun, J. Wang, J.-G. Zhou, D.-M. Gu, Z.-B. Wang, J. Mater. Chem. 7 (2019) 8302–8314.

- [12] Z. He, Z. Wang, H. Chen, Z. Huang, X. Li, H. Guo, R. Wang, J. Power Sources 299 (2015) 334–341.
- [13] Y. Lyu, N. Zhao, E. Hu, R. Xiao, X. Yu, L. Gu, X.-Q. Yang, H. Li, Chem. Mater. 27 (2015) 5238–5252.
- [14] C.S. Johnson, J.S. Kim, A.J. Kropf, A.J. Kahaian, J.T. Vaughey, L.M.L. Fransson, K. Edstrom, M.M. Thackeray, Chem. Mater. 15 (2003) 2313–2322.
- [15] C.S. Johnson, J.S. Kim, A.J. Kropf, A.J. Kahaian, J.T. Vaughey, M.M. Thackeray, Electrochem. Commun. 4 (2002) 492–498.
- [16] G.J. Moore, C.S. Johnson, M.M. Thackeray, J. Power Sources 119 (2003) 216-220.
- [17] Y. Lyu, E. Hu, D. Xiao, Y. Wang, X. Yu, G. Xu, S.N. Ehrlich, K. Amine, L. Gu, X.-Q. Yang, H. Li, Chem. Mater. 29 (2017) 9053–9065.
- [18] K. Jeom-Soo, C.S. Johnson, J.T. Vaughey, M.M. Thackeray, S.A. Hackney, Y. Wonsub, C.P. Grey, Chem. Mater. 16 (2004) 1996–2006.
- [19] C.S. Johnson, J.S. Kim, A.J. Kropf, A.J. Kahaian, J.T. Vaughey, M.M. Thackeray, J. Power Sources 119 (2003) 139–144.
- [20] Y.M. Chiang, H.F. Wang, Y.I. Jang, Chem. Mater. 13 (2001) 53-63.
- [21] E. Yin, A. Grimaud, G. Rousse, A.M. Abakumov, A. Senyshyn, L. Zhang, S. Trabesinger, A. Iadecola, D. Foix, D. Giaume, J.-M. Tarascon, Nat. Commun. 11 (2020) 1252.
- [22] P.-F. Wang, M. Weng, Y. Xiao, Z. Hu, Q. Li, M. Li, Y.-D. Wang, X. Chen, X. Yang, Y. Wen, Y.-X. Yin, X. Yu, Y. Xiao, J. Zheng, L.-J. Wan, F. Pan, Y.-G. Guo, Adv. Mater. 31 (2019), 1903483.
- [23] D. Yuan, X. Liang, L. Wu, Y. Cao, X. Ai, J. Feng, H. Yang, Adv. Mater. 26 (2014) 6301–6306
- [24] C. Zheng, X. Zhu, H. Xin, Z. Shao, H. Wang, H. Peng, X. Cheng, F. Wang, Rare Met. Mater. Eng. 48 (2019) 242–248.
- [25] Y. Li, L. Xie, Z. Zheng, Z.-W. Yin, J. Li, M. Weng, J. Liu, J. Hu, K. Yang, G. Qian, B. Cao, Z. Li, S. Xu, W. Zhao, S. Li, J. Sun, M. Zhang, F. Pan, Nano Energy 77 (2020), 105157.
- [26] A.C. Larson, R.B.V. Dreele, General Structure Analysis System (GSAS), LAUR 86-748, Los Alamos National Laboratory, Los Alamos, NM, 2000.
- [27] B.H. Toby, J. Appl. Crystallogr. 34 (2001) 210-213.

- [28] J. Lee, D.A. Kitchaev, D.-H. Kwon, C.-W. Lee, J.K. Papp, Y.-S. Liu, Z. Lun, R. J. Clement, T. Shi, B.D. McCloskey, J. Guo, M. Balasubramanian, G. Ceder, Nature 556 (2018) 185-+.
- [29] C.P. Laisa, A.K.N. Kumar, S.S. Chandrasekaran, P. Murugan, N. Lakshminarasimhan, R. Govindaraj, K. Ramesha, J. Power Sources 324 (2016) 462–474.
- [30] J. Liu, J. Wang, Y. Ni, Y. Zhang, J. Luo, F. Cheng, J. Chen, Small Methods 3 (2019), 1900350.
- [31] H.A. Mueller, Y. Joshi, E. Hadjixenophontos, C. Peter, G. Csiszar, G. Richter, G. Schmitz, RSC Adv. 10 (2020) 3636–3645.
- [32] M.A. Cambaz, B.P. Vinayan, H. Euchner, R.E. Johnsen, A.A. Guda, A. Mazilkin, Y. V. Rusalev, A.L. Trigub, A. Gross, M. Fichtner, ACS Appl. Mater. Interfaces 10 (2018) 21957–21964.
- [33] M. Zhang, Z. Li, L. Yu, D. Kong, Y. Li, B. Cao, W. Zhao, J. Wen, F. Pan, Nano Energy 77 (2020), 105188.
- [34] J. Zheng, Y. Ye, F. Pan, Natl. Sci. Rev. 7 (2020) 242. -+.
- [35] Z. Zheng, M.-Y. Weng, L.-Y. Yang, Z.-X. Hu, Z.-F. Chen, F. Pan, Chin. J. Struct. Chem. 38 (2019) 2020–2026.
- [36] Z. Hu, M. Weng, Z. Chen, W. Tan, S. Li, F. Pan, Nano Energy 83 (2021), 105834.
- [37] Y.-K. Hou, G.-L. Pan, Y.-Y. Sun, X.-P. Gao, ACS Appl. Energy Mater. 1 (2018) 5703–5711.
- [38] M.J. Wang, F.-D. Yu, G. Sun, D.-M. Gu, Z.-B. Wang, ACS Appl. Energy Mater. 1 (2018) 4158–4168.
- [39] Y. Liu, P. Wu, F. Liu, F. Li, X. An, J. Liu, Z. Wang, C. Shen, W. Sand, Environ. Sci. Technol. 53 (2019) 1527–1535.
- [40] Y. Yang, H. Su, T. Wu, Y. Jiang, D. Liu, P. Yan, H. Tian, H. Yu, Sci. Bull. 64 (2019) 553–561.
- [41] D. Ye, G. Zeng, K. Nogita, K. Ozawa, M. Hankel, D.J. Searles, L. Wang, Adv. Funct. Mater. 25 (2015) 7488–7496.
- [42] S. Muhammad, H. Kim, Y. Kim, D. Kim, J.H. Song, J. Yoon, J.-H. Park, S.-J. Ahn, S.-H. Kang, M.M. Thackeray, W.-S. Yoon, Nano Energy 21 (2016) 172–184.
- [43] J.-L. Shi, J.-N. Zhang, M. He, X.-D. Zhang, Y.-X. Yin, H. Li, Y.-G. Guo, L. Gu, L.-J. Wan, ACS Appl. Mater. Interfaces 8 (2016) 20138–20146.